Coupling the structure evolution and the oxygen redox electrochemistry in layered transition metal oxides

Donggun Eum
Seoul National University
Byunghoon Kim
Seoul National University
Jun-Hyuk Song
Seoul National University
Hyeokjun Park
Seoul National University https://orcid.org/0000-0003-3367-8881
Sung Joo Kim
Brookhaven National Laboratory
Sung-Pyo Cho
Seoul National University
Ho-Young Jang
Seoul National University
Myeong Hwan Lee
Seoul National University
Jae Hoon Heo
Seoul National University
Youngmin Ko
Seoul National University
Sung Kwan Park
Seoul National University
Kyungbae Oh
Seoul National University
Do-Hoon Kim
Seoul National University
Kisuk Kang (matlgen1@snu.ac.kr)
Seoul National University https://orcid.org/0000-0002-8696-1886

Article

Keywords: layered transition metal oxides, oxygen redox electrochemistry, rechargeable batteries

Posted Date: January 13th, 2021

DOI: https://doi.org/10.21203/rs.3.rs-142599/v1

Version of Record: A version of this preprint was published at Nature Materials on March 17th, 2022. See the published version at https://doi.org/10.1038/s41563-022-01209-1.

Abstract

Lattice oxygen redox activity offers an unexplored way to access the latent superior electrochemical property of transition metal oxides for rechargeable batteries. However, the redox reaction of the lattice oxygen is often accompanied by unfavorable structural transformations and the corresponding degradation of electrochemical performances, precluding its practical application. Herein, we explore the close interplay between the local structural change during the dynamic intercalation process and the solid-state oxygen electrochemistry in the short- or long-term battery operation for layered transition metal oxides. By employing two model systems of the layered $Na_{0.6}(Li_{0.2}Ti_xMn_{0.8-x})O_2$ with the oxygen redox capability, it is demonstrated that the substantially distinct evolutions in the oxygen redox activity and reversibility are caused by different cation migration mechanisms available in the system during the de/intercalation (*i.e.* out-of-plane and in-plane migrations of transition metals (TMs)). We show that the π stabilization upon the oxygen oxidation initially aids in the reversibility of the oxygen redox and is predominant in the absence of TM migrations, however, the π-interacting oxygens are gradually replaced by the σ-interacting oxygens that trigger the formation of O–O dimers and the structural destabilization over cycles. More importantly, it is revealed that the distinct TM migration paths available in the respective layered materials govern the conversion from π to σ interactions and its kinetics. It infers that regulating the dynamics of TMs in the layered materials can play a key role in delaying or inhibiting the deterioration of the oxygen redox reversibility. These findings constitute a step forward in unraveling the correlation between the local structural evolution and the reversibility of solid-state oxygen electrochemistry, and provide a guidance for developing oxygen-redox layered electrode materials.

Main Text

The use of reversible lattice oxygen redox has been a transformative strategy for accessing superior electrochemical activity of transition metal oxide-based materials such as in catalysts and battery electrodes.[1–3] In particular, with the growing demands for the next-generation battery technology, extensive efforts have been devoted to exploiting the lattice oxygen redox in developing novel electrode materials with higher energy densities. Lithium-rich layered oxides ($Li_{1+x}TM_{1-x}O_2$, TM: transition metal) are one of the examples, which could exhibit the remarkable oxygen redox activity.[4,5] The cumulative cationic and anionic redox activities from TM and oxygen, respectively, enable them to deliver energy and power densities that can surpass those of conventional lithium layered oxides ($LiTMO_2$). More recently, various transition metal oxides have been investigated as being capable of showing the anionic redox activity, which include not only lithium-rich layered compounds but also sodium layered oxides, disordered rocksalt phases, partially ordered spinels and anti-fluorite compounds.[6–11] The variety of material groups found for the anionic redox activity suggests that the lattice oxygen redox can be universally attainable and be certainly a way to further improve the electrochemical activity of battery electrodes in general.

Despite the disputes regarding the origin of the lattice oxygen redox, a clear consensus has been reached that a specific oxygen 2*p* state, which is generated by the TM-deficient environment around oxygen in A-rich layered materials (A: Li, Na, Mg, and vacancy), plays a pivotal role in electrochemically activating the lattice oxygen.[12–15] In principle, such an ionic state is similar to a non-bonding state because of the weak hybridization of the O 2*p* orbital through the A–O–A configuration, and thus, the extraction of electrons from the oxygen band becomes energetically feasible, allowing the oxygen redox in the conventional electrochemical operation window.

Nonetheless, we note that such a local configuration of oxygen that enables the redox activity is not likely to be always preserved during the dynamic intercalation process, and various studies have experimentally reported substantial evidences of structural transitions involving significant cation migrations around oxygen after electrochemical cycles.[16–20] Chueh and co-workers demonstrated that a TM–oxygen decoordination process could occur inducing the change in the oxygen coordination, and discussed the possible effect of cation migrations on the oxygen redox in $Li_{1.17}Ni_{0.21}Co_{0.08}Mn_{0.54}O_2$[16] and $Li_2Ir_{0.75}Sn_{0.25}O_3$[17]. Also, recent theoretical investigations of oxygen redox proposed that localized holes on oxygen are expected to be stabilized to follow the universal octet rules by TM–O coupling or O–O pairing.[21,22] In this case, the local coordination of oxygen undergoes noticeable changes via π or σ interactions with neighboring TM or oxygen. The substantial structural rearrangements were also witnessed in various kinetic studies of the anionic redox reaction.[18,23,24] It was emphasized that the anionic redox is accompanied by the local structural changes such as O–O dimerization or TM migration, causing the voltage hysteresis and sluggish kinetics simultaneously.[23,24] In addition, such massive TM migration was recently alleged to cause sluggish lithium diffusion rate during the electrochemical cycling.[18] These series of findings indicate that the initial condition of the oxygen redox with respect to the coordination is not constantly maintained, and imply that the reversibility of the oxygen redox can be easily jeopardized. Although numerous attempts have been made to elucidate the general nature of the oxygen redox[15–17, 21,25–28], the clear-cut explanation on the interplay among the structural stability/transition kinetics and the reversibility/kinetics of oxygen redox has yet to be established particularly for the 3*d*-metal-based layered oxides of practical interest.

Noteworthy is that recent works identified series of layered oxides that could maintain the structural integrity remarkably well with the reversible anionic redox (*e.g.* P-type layered structures).[29–31] It was proposed that in the P-type structure[32], unlike conventional lithium layered oxides, TM ions do not migrate to the interlayer space because of the instability of TM ions in the prismatic sites in the layer, thus the structural change is effectively minimized. It implies that these layered materials can serve as an ideal platform to inspect the intrinsic oxygen-redox chemistry excluding the effect of TM migrations, or, in other words, to systematically investigate the effect of TM migrations, if can be intentionally induced, on the lattice oxygen redox. In this work, we selected two model P-type layered sodium oxides; one that has been previously reported to be structurally stable with the anionic redox, $Na_{0.6}(Li_{0.2}Mn_{0.8})O_2$ (NLMO), and the other that undergoes a noticeable structural evolution with the anionic redox, $Na_{0.6}(Li_{0.2}Ti_{0.2}Mn_{0.6})O_2$

(NLTMO), while both being in the same P-type layered structure with the identical transition metal/lithium ordering (ribbon-like ordering) in the lithium-containing TM layer. We show that the substantially distinct evolutions in the oxygen redox activity and reversibility are observed for the two samples during the cycles, and reveal that the evidently different behaviors arise from the two dissimilar TM-migration mechanisms; (i) rapid out-of-plane disordering (NLTMO) and (ii) slowly-occurring in-plane disordering (NLMO). It is further verified that the TM-migration modes are closely coupled with the change in the oxygen stabilization mechanism from the π stabilization to the σ-interacting oxygens that trigger the formation of O–O dimers and the structural destabilization over cycles. The correlation among the distinct TM migration path, the formation of the O–O dimers and the oxygen redox stability will be extensively discussed in the comparative analysis of the two model materials.

Redox activity of the lattice oxygen in layered structures

NLMO and NLTMO both adopt a P3-type layered structure with the alternative stackings of sodium layer and TM layer (partially containing lithium)[33], as schematically illustrated in Fig. 1a. Because of the unique 1:4 ratio between the lithium and TM ions, the ribbon-like ordering is present in the TM layer, which is confirmed by the superstructure peaks observed for both materials in high-resolution powder diffraction (HRPD) measurements (see dotted boxes and the crystal structure in Fig. 1a and Supplementary Fig. 1–2).[34,35] The initial charging of the two electrodes reveals that the lattice oxygen is the main redox reservoir in the electrochemical system, while the oxidation states of Mn and Ti remain + 4 (Supplementary Fig. 3).[36] Scanning transmission X-ray microscopy (STXM) in Fig. 1b clearly visualizes that, after the charge up to 4.5 V of both materials, a new peak at ~ 531 eV evolves (highlighted region in the figure), providing a solid evidence for the oxidation of the lattice oxygen.[37,38] Despite these similarities in the structure and the initial oxygen oxidation, the electrochemical behavior during the discharge process differs markedly for the two electrodes as presented in Fig. 1c (see Supplementary Fig. 4 together). The high-voltage plateau that was observed for the both electrodes during charge is maintained during discharge only for the NLMO electrode, implying the reversible oxygen redox reaction, whereas it irreversibly transforms into a slanted curve in the NLTMO electrode, exhibiting a large voltage hysteresis of the oxygen redox (see more details in Supplementary Fig. 5). We also found that the change in the oxygen redox makes the kinetic properties significantly altered. Figure 1d and e comparatively illustrate that the oxygen redox in the NLTMO displays notably inferior kinetic performance to that of the NLMO after the initial charging process. While the NLMO electrode retains a respectable rate capability with increasing current densities, the discharge capacities of the NLTMO electrode rapidly decrease presenting increasingly large polarizations with higher current rates. These results suggest that the change in the oxygen redox activity is also accompanied by the kinetic performance degradation of the electrode, in accordance with previous reports.[23,24]

Interestingly, we observed that such an irreversible transition also appears gradually in the charge/discharge profile of the NLMO electrode with the extended cycle numbers, in contrast to the previous findings.[29,34] Fig. 1f displays how the electrochemical profile of the NLMO electrode evolves

with the cycle number, which systematically changes from the flat plateau to the slanted curve that is similar to that of the NLTMO electrode. Eventually, the two profiles of the NLMO and NLTMO electrodes become nearly indistinguishable with the similar average voltage after 30 cycles, as plotted together in Fig. 1g. It implies that the nature of the oxygen redox becomes comparable for the two electrodes after sufficient cycle numbers in contrast to the previous belief regarding the stable oxygen redox activity in the NLMO.[29,34] It also infers that the dissimilar behaviors of the oxygen redox in the NLMO and NLTMO electrodes may be simply rooted from the different rates of the transition or degradation that occurs in the two.

Structural evolutions with distinct TM migration paths

In order to elucidate the changes in the oxygen redox reactions, we comparatively examined the structural evolutions of the NLMO and NLTMO electrodes as a function of the cycles. Figure 2a and b present *ex-situ* HRPD patterns of the NLMO and NLTMO electrodes, respectively, during the first cycle in which each exhibited the similar charge behavior followed by the dissimilar discharge profile. Figure 2a depicts that the NLMO electrode undergoes a notably reversible phase transition during the initial cycle, where the (003) peak at 2θ = 15.7° is reversibly recovered, and the ribbon-like ordering with the superstructure patterns (red shaded) was well preserved after the cycle. A closer inspection of the pattern discloses that the (003) peak at 2θ = 15.7° gradually weakens and a new peak appears at 2θ = 17.3° (denoted with asterisk) with charging, which is characteristic of a two-phase reaction, in accordance with the previous report.[29] Both phases could be indexed as the P3-type layered structure with the *R3m* space group, implying that the layers maintain the prismatic sodium sites even in the desodiated state.[29] In contrast, the patterns of the NLTMO electrode in Fig. 2b illustrate that the (003) diffraction peak gradually shifts to a higher angle of 17.9° without an emergence of a new peak during charge, which is reversed during the discharge. It was previously discussed that the de-/sodiation of the Ti or Fe-doped P-type sodium layered materials involves the reversible stacking change, where prismatic sites glide into the octahedral sites, leading to the continuous formation of O-P hybrid layers.[36,39] It suggests that the gradual peak shifts of the NLTMO electrode is attributable to the solid-solution-like behavior arising from the formation of O-P hybrid layered structures upon desodiation. Nevertheless, we noticed that the diffraction patterns of the discharged NLTMO electrode did not fully match with those of the pristine electrode. Specifically, the (003) diffraction peak exhibited a significant peak broadening after a cycle of charge and discharge, showing that the cycled NLTMO is in a highly strained state (see more discussion in Supplementary Fig. 6). More importantly, the ribbon-like ordering of NLTMO in TM layer was lost and converted into a honeycomb-like ordering at 2θ = 22.8° (blue shaded) after the first cycle.[40] It differs from the case of the NLMO as comparatively shown in the magnified views of Fig. 2a and b, which implies that a substantial TM migration has occurred during the dynamic intercalation process of the NLTMO electrode. It is also noteworthy that it is in contrast to the previous finding that the ribbon-like ordering in TM layer generally prohibits the migration of TMs in the structure, aiding in the reversible oxygen redox.[35]

Raman spectroscopy analysis was further performed to verify the TM migrations and the corresponding TM–O bonding characters of the NLMO and NLTMO electrodes in Fig. 2c and e, respectively. It has been

widely known that the peak at 636.5 cm^{-1} is a signature of symmetric stretching (A_{1g}) of the TM–O bond in layered structures, whereas the peak at 580 cm^{-1} arises from asymmetric stretching (E_{2g}) of the Na–O bond.[41] Fig. 2c depicts that the A_{1g} TM–O vibration mode denoted with circle is preserved without any additional peaks for the first cycle of the NLMO electrode, which is indicative of the unaltered TM–O nature, while the Na–O E_{2g} peak changes its intensity simply with de-/sodiation. Notably, this finding contrasts to the case of the NLTMO in Fig. 2e, where a new shoulder peak at 688 cm^{-1} (denoted with rhombus) appears and disappears reversibly during the successive charge and discharge. According to previous studies, the new peak with a higher wavenumber of TM–O vibrations is attributed to the substantial out-of-plane cation disorder with a new TM coordinating environment.[20,42] It suggests that the charge/discharge of the NLTMO electrodes involves the out-of-plane migration of TMs in the P-type layered structure, which is not observed in the similarly structured NLMO electrode.

The presence of the out-of-plane TM migrations with the electrochemical cycle could be more closely investigated by comparatively conducting spherical-aberration-corrected scanning transmission electron microscopy (Cs-STEM) analysis on the NLMO and NLTMO samples. Figure 2d and f present the high-angle annular dark-field (HAADF) images of the samples in the fully charged states exploiting the Z-contrast imaging.[43,44] For the desodiated NLMO (Fig. 2d), alternating bright TM layers and dark Na layers are clearly observed with an interlayer spacing of 5.55 Å, confirming that the spacing of the prismatic sites is well preserved.[45,46] It supports the observation from the Raman spectroscopy that the out-of-plane cation disorder does not take place in the NLMO electrode after the initial charging. On the other hand, a noticeable amount of TM ions was found to occupy the vacant Na sites in the desodiated NLTMO (denoted with the arrows in Fig. 2f). Moreover, some of the interlayer spacings were estimated to be 4.61 Å, which is markedly smaller than 5.55 Å and corresponds to the typical values observed for the O-type layers with the octahedral environments.[26,47] It indicates that the charged state of the NLTMO adopts the O-P hybrid layered structures[36], where the occupancy of TM in the Na layer is likely to induce the O-type layers. We also speculate that the loss of the ribbon-like ordering in TM layer observed in Fig. 2b is partly attributable to the substantial out-of-plane migrations of the TM ions. The extra vacancies in the TM layers owing to the out-of-plane migrations would provide sufficient vacant sites for the in-plane cation (Li/TM) redistributions upon the initial charging, causing the loss of the initial ribbon-like orderings and the formation of the honeycomb-like orderings.

Effect of TM migrations on the oxygen redox

Inspired by the distinct behaviors of TM migrations observed for the two electrodes, we attempted to gain further insights in the influence of the TM migrations on the oxygen redox by the theoretical considerations of the electronic and magnetic structures. When the lattice oxygen gets oxidized, the holes are created, yielding the unpaired electrons in the orphaned oxygen 2*p* states. The change in the electronic/magnetic structure can subsequently occur via various types of interactions with neighboring oxygens and TMs, which involves dynamic electron transfer.[22] We deduce that the oxidized oxygen in lattice can be in a state of (i) non-stabilized oxygen, (ii) π-stabilized oxygen, or (iii) σ-stabilized oxygen,

which would accompany localized holes, delocalized holes by TM–O coupling, or delocalized holes by O–O dimerization, respectively, as schematically illustrated in Fig. 3a. According to previous works[14,30,48], the π-stabilization is readily formed between the oxygen and the neighboring TM in the pristine layered structure due to the intrinsic directional coordination involving oxygen 2*p* and TM 3*d* orbitals. However, it is noteworthy that, when the out-of-plane TM migrations occur, density functional theory (DFT) calculations revealed the TM–O decoordination that is usually accompanied by the TM migration strongly promotes the σ-stabilized O–O dimerization. Figure 3b illustrates that the dangling oxygen ion is generated near the vacant TM defect sites, weakening the potential π-stabilization between the oxygen and TMs. Moreover, it was found that short oxygen dimers are subsequently induced with the lengths of 1.35 and 1.42 Å in the vicinity of the out-of-plane TM migration. Considering the significant TM migration observed in the desodiated NLTMO electrode, a substantial number of single- or even non-coordinated oxygens are expected to evolve during charging, which would likely form the short oxygen dimers with the adjacent oxygen ions for the stabilization.

The change in the oxygen nature could be further supported by the comparative magnetic measurements of the charged NLMO and NLTMO electrodes using a superconducting quantum interference device (SQUID).[49,50] Supplementary Fig. 7 shows the temperature dependence of the reciprocal magnetic susceptibility in the NLMO and NLTMO electrodes. Through Curie–Weiss fitting of the susceptibility curves between 180 K and 250 K, the effective magnetic moments of two electrodes were extracted as a function of the state of charge (SOC) and plotted in Fig. 3c and d. The magnetic moments of the pristine NLMO and NLTMO electrodes were measured to be 3.94 and 3.92 μ_B, respectively; these values are close to the expected value of the high-spin Mn^{4+} ions (3.87 μ_B), confirming that the oxidation states of Mn ions are close to + 4 in both pristine electrodes.[51] Upon charging (*i.e.* oxygen oxidation), however, two electrodes exhibited the opposite behavior in the change of the effective magnetic moments with the SOCs. Noteworthy is that the magnetic moment of the NLTMO increases with two positive slopes along with the oxygen oxidation, whereas that of the NLMO decreases with a constant slope, indicative of the distinguishing nature in the electronic structure evolutions of the two electrodes with charging. It clearly manifests the contrasting oxygen stabilization mechanisms in the two systems, considering the relationship between the electronic structure expected for the possible oxygen states and the magnetic moments of the materials (see detailed explanations on the expected magnetic moments with different types of oxygen states in the caption of Fig. 3a). Moreover, the quantitative analysis of the slopes in Fig. 3c and d could offer more detailed picture of the oxygen stabilization process during the charge. Based on the slopes observed in the plot, the fraction of the aforementioned types of oxidized oxygens could be quantitatively deconvoluted for the respective regions of Region 1, Region 2 and Region 3 in Fig. 3c and d, which is depicted comparatively in Fig. 3e. Details on the deconvolution process and the calculations of the fractions are provided in Supplementary Note 1. It reveals that the most prominent interaction in Region 1 is the π-type interaction, which accounts for approximately 62.6% of the oxidized oxygen, suggesting that the majority of oxygen holes in the charged NLMO electrode are likely to be delocalized with the neighboring Mn ions. On the other hand, oxygen holes in the charged NLTMO electrode tend to be delocalized through the σ-interaction of O–O pairing, as indicated with the Region 2

and 3 in Fig. 3e. In particular, during the later charging process of the NLTMO electrode, the fraction of the σ-stabilized oxygen is as high as 95.7%, signifying that almost all the oxygen holes were delocalized through the O–O pairing. This quantitative result is remarkably consistent with our theoretical calculations, which suggested that the out-of-plane TM migration in the NLTMO induces the subsequent oxygen dimerization between the adjacent lattice oxygens. The results here imply the close correlation between the out-of-plane TM migration and the stabilization mechanism of the oxidized lattice oxygen in the layered materials.

We further verified that the stabilized lattice oxygen displays the redox potential that is markedly distinct from that of the pristine non-stabilized oxygen. The partial density of states (pDOS) of oxygen 2*p* orbitals in Fig. 3f shows that the short oxygen dimerization occurring with the TM migration significantly redistributes the electronic structure of the oxygen owing to the strong σ-type O–O interaction. The pristine non-bonding O_{2p} states are reorganized into sharp and discrete states corresponding to σ-type O–O bond, thereby lifting the overall oxygen states from below to far above the Fermi level. Considering that the shifted O–O states are located at far higher energy states than the minimum of empty (Mn–O) e_g* states, as highlighted in the DOS of Fig. 3g, a partial manganese reduction prior to complete oxygen reduction is expected upon discharge process. Notably, this speculation could be experimentally confirmed through our X-ray absorption near edge spectroscopy (XANES) analysis. Figure 3h and i present the Mn K-edge absorbance spectra of the NLMO and NLTMO electrodes, respectively, during the successive charge and discharge process. It shows that the Mn edge position of the NLTMO is maintained initially, however, upon discharge to 2.0 V, shifts toward a lower energy close to that of the $Mn^{3+}{}_2O_3$ reference, accounting for the partial reduction of Mn^{4+} to Mn^{3+} in the low-voltage region, while that of the NLMO does not shift from the initial oxidation state of Mn^{4+} over the entire voltage range. It is a remarkable agreement with the results of the DOS in Fig. 3g, and is attributed to the oxygen stabilization mechanism in the presence of the TM migration, *i.e.* O–O pairing. It is supposed that the reversed electronic states of the fully charged states of NLTMO eventually induces the detour of the thermodynamic path in the discharging process, triggering the voltage hysteresis. Moreover, since the dimer formation entails structural rearrangements involving TM migrations, the kinetic properties would become comparatively sluggish, elucidating the inferior rate performance of the NLTMO electrode in Fig. 1e. It suggests that the oxygen stabilization mechanism has a crucial influence on the thermodynamic and kinetic properties of the oxygen redox in the layered materials.

Gradual formation of oxygen dimers in LNMO and its direct visualization

Despite the seemingly intact structural stability, the NLMO electrode also eventually exhibited the degradation of the electrochemical profile with the voltage fades as depicted in Fig. 1f and g. In this regard, we carefully re-examined the structural evolution of the NLMO electrode over the extended cycles. Figure 4a presents *ex-situ* HRPD patterns and Raman spectra of the 1, 10 and 30 cycled NLMO electrodes at the fully charged states, where significant out-of-plane TM migrations have been observed in the NLTMO counterpart. It shows that the characteristic two phase reaction of the NLMO is consistently retained, clearly exhibiting the two (003) peaks at 2θ = 15.7 and 17.3° at the charged state, over the 30

cycles, which differs from the O-P hybrid structure formation of the NLTMO involving the significant TM migrations. Moreover, the signature of the out-of-plane TM migrations such as a shoulder peak at 688 cm^{-1} does not appear even after the 30 times of the charging in the Raman spectra. Cs-STEM characterization in Supplementary Fig. 12 also supported that the P-type layered structure was well preserved for the NLMO electrode even after 30 cycles, implying the absence of the out-of-plane TM migration either at charged or discharged states for the 30 cycles. Nevertheless, we observed that the (003) peak intensities notably decrease with the extended cycling from the HRPD patterns, exhibiting the gradual loss of the crystallinity. Supplementary Fig. 13 illustrates that the full width at half maximum (FWHM) of the 30-cycled electrode is noticeably greater than that of the initial electrode. More importantly, it was found that the superstructure peaks corresponding to ribbon-like ordering in TM layer completely disappeared after 30 cycles, as shown in Fig. 4b. These results suggest that substantial TM migrations other than the out-of-plane migration have occurred and caused the partial structural inhomogeneity, strongly implying the presence of the in-plane TM migrations in the TM layer. It is also noteworthy that the lithium contents in the TM layer progressively decreased upon cycling, as presented in Fig. 4c (see more details in Supplementary Tables 2–3). It indicates that sufficient vacant sites in the TM layer were created especially at the later cycles, which would facilitate the in-plane TM migration and the subsequent disordering of the TM layer. This speculation could be supported by the additional experiments provided in Supplementary Note 2, in which we found that in-plane migration is critically dependent on the lithium/vacancy (Li/V) concentrations in the TM layer.

To further probe the TM layer rearrangements in the NLMO, the extended X-ray absorption fine structure (EXAFS) analysis of the 1-, 10-, 20-, and 30-cycled electrodes was additionally conducted (Supplementary Fig. 19). Characteristic peaks of the first and second shells in the Mn K-edge data, which correspond to the closest manganese–oxygen ($Mn–O_6$) and manganese–metal ($Mn–M_6$; M: Li or Mn in the same layers) bonds, respectively, were fitted with the P3-type model structure (Supplementary Table 5). Figure 4d depicts the fitted values of the Debye–Waller factor, which is indicative of the structural disorder, for every 10 cycles. The results indicate that the Debye–Waller factor of the $Mn–M_6$ shell continuously increases with cycling, supporting that the in-plane disordering in the TM layer takes place gradually. The factor of the $Mn–O_6$ shell, on the other hand, remained nearly constant for the electrochemical cycling. It signifies that the overall P-type layered structure is relatively well preserved over the cycling, in consistent with the HRPD results, even when the substantial disordering occurs within the TM layer. The gradual in-plane disordering in the TM layer was found to accompany a noticeable rearrangement of the electronic structure of the NLMO, displaying a continuous shift of the Mn K-edge spectra in Fig. 4e. The apparent reduction of the Mn in the NLMO at later cycles is reminiscent of the case of the NLTMO wherein the oxidized oxygens were stabilized by O–O pairing, causing the reversed electronic states at the fully charged states as elucidated in Fig. 3i and g of NLTMO. It implies that the in-plane anti-site defects in the TM layer has also induced the gradual oxygen dimerization in the NLMO, as will be discussed further in the following.

The clear evidence of the oxygen dimers could be obtained from the annular bright-field (ABF) STEM images taken for the charged NLMO electrodes after 30 cycles, in comparisons with that at the first cycle as presented in Fig. 4f and g.[52,53] Along the [010] zone axis, alternating MnO_6 layers and vacant Na layers could be visibly projected. The ABF image for the first charged electrode in Fig. 4f reveals a highly ordered structure of the NLMO, where the manganese and oxygen atomic features are evidently spotted and well aligned along the axis. In contrast, the charged electrode after 30 cycles in Fig. 4g manifests that the oxygen signals around the TM columns are relatively weaker in the intensity than those in the first charged sample, indicating that the oxygen sites are significantly distorted. According to our findings and the previous observations of the lattice distortion of oxygen-redox materials[26,54], it suggests that various oxygen bonding environments have been generated after the 30 cycles. The lattice distortion over the oxygen regions is more obviously confirmed by the signal profiles along the horizontal direction in the inset of Fig. 4f and g, displaying additional oxygen peaks for the sample after 30 cycles. Contrary to the charged NLMO at the first cycle, where the single oxygen peak is clearly observed, the oxygen peaks could be indexed apparently by two Gaussian functions, indicating that the distorted signals can be attributed to the two oxygen atoms with the unusually short distance, *i.e.* oxygen dimers.

To further assign the features of the oxygen dimers, we carried out Raman analysis to estimate the bonding lengths between the oxygens from the vibrational frequency.[55.56] While the direct measurement of the short oxygen bond length (< 1.34 Å) has not yet been achieved for battery electrodes, to the best of our knowledge, previous Raman studies on a variety of metal complexes containing O–O collectively suggested that the presence of the short oxygen dimers display the characteristic vibration frequency in the range of 1100 and 1500 cm^{-1}.[55] It is also noteworthy that its detection has been generally ambiguous because the strong D and G bands at 1350 and 1587 cm^{-1} of the carbon additives in the electrode screen the signals from short oxygen dimers.[57] In this respect, we measured the electrode without carbon effects (see Supplementary Note 3 for details) and performed the analysis as presented in Fig. 4h. Two characteristic peaks were clearly discerned at 1164.7 and 1292.2 cm^{-1}, as denoted with the green area, which correspond to the oxygen dimers with the distance of 1.28 and 1.33 Å.[35,55] The measured oxygen dimer distance is in a reasonable agreement with our DFT calculations (*i.e.* 1.35 and 1.42 Å) in Fig. 3b when the TM migration was considered. Additionally, we could detect a low-frequency peak at 477.7 cm^{-1}, which is attributed to the TM–(O–O) vibration, demonstrating the simultaneous formation of $Mn–O_2$ configurations.[58.59] Its detection further supports the formation of the oxygen dimers in the cycled NLMO electrode. Moreover, it proposes that the oxygen that loses its coordination due to the TM migration tends to bind to the adjacent O–Mn configuration, implying the correlation between the metal–oxygen decoordination and the formation of the oxygen dimers. Interestingly, we found that the integrated intensities of both O–O and TM–(O–O) signals continuously increase upon repeated cycles, as illustrated in Fig. 4i. This systematic increase of the dimer-related vibration peaks with cycles indicates that more oxygen dimers are produced along with the cycle numbers in consistent with our structural analysis results. It is attributable to that the progressive in-plane TM migration in the NLMO

assists the oxygen dimerization upon repeated cycling, as supported by our further theoretical calculations (Supplementary Note 4).

Overall, the characterization of the NLMO electrode unequivocally confirms that the gradual transition of the oxygen chemistry is caused by the progressively occurring in-plane TM movements, while the rapid out-of-plane TM migration dominated the structural evolution of the NLMTO electrode. As discussed in Fig. 4c, the in-plane TM migration is coupled with the Li/V concentration and promoted by the sufficient number of vacant sites in TM layer. Since the electrochemical cycles of the NLMO electrode would inevitably involve the partial extraction of lithium ions from the structure at every cycle, it explains why the in-plane TM migration is accelerated with the cycle number. It also implies that the Li substitution itself in the TM layer, which is essential to form the non-bonding state for the oxygen redox activity, can exhibit the adverse effects to some extent on the reversibility of the oxygen redox reaction, thus the trade-off relationship needs to be carefully considered. The contrasting structural and electrochemical behaviors of the two model systems unveil how different cation disordering mechanisms are associated with the oxygen network reorganization and the corresponding evolution of the oxygen redox activity. Our findings thus establish a clearer picture of the structure-property relationships for the solid-state oxygen electrochemistry in the layered transition metal oxide electrodes.

In summary, we demonstrated the strong interrelationship between the lattice oxygen redox and local structural change during the dynamic intercalation process in TM-oxide-based electrodes by comparing two analogous materials with substantially different oxygen redox activity and stability resulting from distinct structural behaviors. It was found that the irreversible electrochemistry of lattice oxygen in the NLMO and NLTMO electrodes exclusively originates from distinct TM migration paths (*i.e.* in-plane and out-of-plane cation migration, respectively), as confirmed by HRPD, STEM, Raman spectroscopy, and complementary EXAFS measurements. Such cation migration eventually leads to the formation of short O–O dimers (< 1.34 Å), thereby stabilizing the oxygen network through rearrangement of the electronic structures. Two types of stabilization mechanisms for the oxidized oxygen and their relevance to the electrochemical behaviors were elucidated through the theoretical investigations of the electronic and magnetic structures. Furthermore, because of the structural simplicity of NLMO even in the disordered state, the O–O dimers were directly observed using ABF-STEM, and their bonding lengths with TM–(O–O) configurations were concomitantly identified using Raman spectroscopy. This work provides a clearer view of oxygen-redox chemistry in relation with the local structure/transition, and hints at robust design guidelines for resolving the issues of voltage hysteresis and sluggish kinetics in oxygen-redox materials. Our findings indicate that regulating the TM migration and its pathway is vital for tailoring the oxygen stabilization mechanism and subsequently achieving highly stable and reversible anionic redox chemistry.

Methods

Synthesis. P3-$Na_{0.6}(Li_{0.2}Mn_{0.8})O_2$ and P3-$Na_{0.6}(Li_{0.2}Ti_{0.2}Mn_{0.6})O_2$ were synthesized by conventional solid-state synthesis. Stoichiometric amounts of Na_2CO_3 (>99%, Sigma–Aldrich), Li_2CO_3 (99.99%,

Sigma–Aldrich), MnO_2 (> 99%, Sigma–Aldrich), and TiO_2 (> 99%, Sigma–Aldrich) were mixed homogeneously with acetone for 24 h. The resultant mixture was stirred over 12 h at room temperature to evaporate the acetone. The final products were obtained by heating the collected powder at 500 °C for 5 h and 650 °C for 24 h with intermediate grinding.

Electrochemistry. A slurry of 80 wt% active materials, 10 wt% carbon black (Super P), and 10 wt% polyvinylidene fluoride dissolved in *N*-methyl-2-pyrrolidone (NMP; 99.5%, Sigma–Aldrich) was cast onto aluminum foil to fabricate the electrodes. The mixture was dried in a 70 °C vacuum oven overnight to evaporate the NMP solution. Coin cells (CR2032, Hohsen) and Swagelok-type cells were assembled using the electrodes, a sodium counter electrode, a separator (GF/F filter, Whatman), and a 1 M solution of $NaPF_6$ in a mixture of ethyl carbonate and dimethyl carbonate (EC/DMC, 1:1 v/v) or propyl carbonate (PC) in an Ar-filled glove box. The PC electrolyte was only used for the DEMS measurement because of the volatility of the EC/DMC electrolyte. The galvanostatic charge/discharge process was performed in the voltage range of 2.0–4.5 V at room temperature.

HRPD. High-resolution powder diffraction was performed at beamline 9B of the Pohang Light Source (PLS) at the Pohang Accelerator Laboratory (PAL), Republic of Korea. The data were collected over the 2 range of 10°–133° with a step size of 0.02°, step time of 3 s, and wavelength of =1.5225 Å. Rietveld refinement of the HRPD patterns was performed using the FullProf program.

Raman spectroscopy. Raman spectra were recorded using a Raman spectrometer (LabRAM HV Evolution, HORIBA) with an Ar laser as the excitation light source (=532 nm). The scattered light of the Raman signal was collected in a backscattering geometry using a 50× microscope objective lens. The data were collected using an acquisition time of 15 s with 10 accumulations. The spectra were deconvoluted using the XPS Peak program.

Cs-STEM. Cross-sectional TEM specimens of the electrode slurry films were prepared using focused ion beam (FIB) milling (Helios 650, FEI). The prepared specimens were used for HAADF and ABF imaging under 200 keV using aberration-corrected STEM (JEM-ARM200F, JEOL) with a point-to-point resolution of 0.08 nm at the National Center for Inter–university Research Facilities (NCIRF) at Seoul National University.

SQUID. For the magnetic characterization, a powder cell using a Swagelok-type cell with an 8:2 ratio of active materials to carbon black was tested. The magnetic properties of the collected powder samples were recorded using a SQUID magnetometer (MPMS-VSM, Quantum Design) at the Korea Basic Science Institute (KBSI). The magnetic moments were measured using a zero-field cooling process from 300 K to 5 K. The field was fixed at 0.1 T during the process.

DEMS. The real-time gas evolution was detected and analyzed with a mass spectrometer (MS; HPR-20, Hiden Analytical) during the cell testing. A controlled amount of Ar flow swept the evolved gas from the Swagelok-type cell to the MS chamber. During cell operation, the pressure inside the MS chamber was maintained at 9.9×10^{-7} Torr.

XANES. XANES spectra of the harvested electrodes were obtained at beamline 7D of the PLS using a double-crystal monochromator containing two sets of Si(111) crystals. All the measurements were performed at room temperature, and the Ti and Mn K-edge spectra were collected in transmission mode. To accurately calibrate the energy scale and any drift of the monochromator position, metal foils were placed in a third chamber as a reference. All of the spectra were normalized and compared using the Athena and Artemis programs.

STXM. STXM analysis was performed at beamline 10A of the PLS to obtain the O K-edge spectra. Primary particles were drop-cast onto carbon-coated Cu TEM grids for the measurements. By maintaining the focal position at the same particle, the two-dimensional transmitted photon intensity was recorded in pixel form at a fixed energy. To obtain image stacks, the same measurements were repeated over different X-ray energy ranges. The image stacks were acquired in 0.2-eV steps with a 2-ms dwell time and were aligned using the aXis 2000 software package.

First-principles calculations. All the *ab initio* calculations were spin-polarized based on density functional theory (DFT), as implemented in the Vienna *ab initio* simulation package (VASP).[61] Structural relaxations were conducted within the Perdew–Burke–Ernzerhof (PBE) generalized gradient approximation.[62] The rotationally invariant Dudarev method was applied, and an effective Hubbard-*U* parameter (3.9 for 3*d* electrons of Mn) was selected based on a previous report.[63] All the structures were fully relaxed until the interatomic forces converged to less than 0.02 eV $Å^{-1}$. A plane-wave cutoff of 520 eV was applied along with a well-converged k-point grid for each system. Detailed information on the model construction and TM migration analysis is provided in Supplementary Note 5.

Declarations

Acknowledgements

This work was supported by the National Research Foundation of Korea (NRF) grant funded by the Korea government (MSIP) (No. 2018R1A2A1A05079249), and Creative Materials Discovery Program through the National Research Foundation of Korea (NRF) funded by the Ministry of Science, ICT and Future Planning (NRF-2017M3D1A1039553). This research was supported by Project Code (No. IBS-R006-A2) and the research program of LG Chem.

Author contributions

D.E. and K.K. conceived of the basic idea for this project and led the research. D.E. performed the material synthesis, electrochemical testing, and structural/spectroscopic characterization including DEMS, HRPD, XANES, STXM, and Raman analyses. B.K. conducted the DFT calculations. B.K., J.-H.S., H.P., and H.-Y.J. discussed and provided fundamental ideas for the overall study. S.J.K. and S.-P.C. performed the STEM measurements, and S.J.K. contributed to the interpretation of the results. M.H.L. and J.H.H. provided constructive advice for the experimental design for the structural characterization. H.-Y.J. and Y.K. assisted with processing of the SQUID and DEMS results, respectively. S.K.P., K.O., and D.-H.K. offered

valuable comments for this project. D.E. and K.K. wrote the manuscript, and K.K. supervised all aspects of the research.

Competing interests

The authors declare no competing interests.

References

1 Grimaud, A. *et al.* Activating lattice oxygen redox reactions in metal oxides to catalyse oxygen evolution. *Nat. Chem.* **9**, 457-465 (2017).

2 Grimaud, A., Hong, W. T., Shao-Horn, Y. & Tarascon, J. M. Anionic redox processes for electrochemical devices. *Nat. Mater.* **15**, 121-126 (2016).

3 Sathiya, M. *et al.* Reversible anionic redox chemistry in high-capacity layered-oxide electrodes. *Nat. Mater.* **12**, 827-835 (2013).

4 Assat, G. & Tarascon, J.-M. Fundamental understanding and practical challenges of anionic redox activity in Li-ion batteries. *Nat. Energy* **3**, 373-386 (2018).

5 Li, B. & Xia, D. Anionic Redox in Rechargeable Lithium Batteries. *Adv. Mater.* **29**, 1701054 (2017).

6 Kim, D., Cho, M. & Cho, K. Rational Design of $Na(Li_{1/3}Mn_{2/3})O_2$ Operated by Anionic Redox Reactions for Advanced Sodium-Ion Batteries. *Adv. Mater.* **29**, 1701788 (2017).

7 Maitra, U. *et al.* Oxygen redox chemistry without excess alkali-metal ions in $Na_{2/3}[Mg_{0.28}Mn_{0.72}]O_2$. *Nat. Chem.* **10**, 288-295 (2018).

8 Lee, J. *et al.* Reversible Mn2+/Mn4+ double redox in lithium-excess cathode materials. *Nature* **556**, 185-190 (2018).

9 Lee, J. *et al.* Mitigating oxygen loss to improve the cycling performance of high capacity cation-disordered cathode materials. *Nat. Commun.* **8**, 981 (2017).

10 Ji, H. *et al.* Ultrahigh power and energy density in partially ordered lithium-ion cathode materials. *Nat. Energy* **5**, 213-221 (2020).

11 Zhan, C. *et al.* Enabling the high capacity of lithium-rich antifluorite lithium iron oxide by simultaneous anionic and cationic redox. *Nat. Energy* **2**, 963-971 (2017).

12 Luo, K. *et al.* Charge-compensation in 3*d*-transition-metal-oxide intercalation cathodes through the generation of localized electron holes on oxygen. *Nat. Chem.* **8**, 684-691 (2016).

13 Seo, D.-H. *et al.* The structural and chemical origin of the oxygen redox activity in layered and cation-disordered Li-excess cathode materials. *Nat. Chem.* **8**, 692-697 (2016).

14 Song, J.-H. *et al.* Anionic Redox Activity Regulated by Transition Metal in Lithium-Rich Layered Oxides. *Adv. Energy Mater.* **10**, 2001207 (2020).

15 Xie, Y., Saubanère, M. & Doublet, M. L. Requirements for reversible extra-capacity in Li-rich layered oxides for Li-ion batteries. *Energy Environ. Sci.* **10**, 266-274 (2017).

16 Gent, W. E. *et al.* Coupling between oxygen redox and cation migration explains unusual electrochemistry in lithium-rich layered oxides. *Nat. Commun.* **8**, 2091 (2017).

17 Hong, J. *et al.* Metal–oxygen decoordination stabilizes anion redox in Li-rich oxides. *Nat. Mater.* **18**, 256-265 (2019).

18 Ku, K. *et al.* A new lithium diffusion model in layered oxides based on asymmetric but reversible transition metal migration. *Energy Environ. Sci.* **13**, 1269-1278 (2020).

19 Yin, W. *et al.* Structural evolution at the oxidative and reductive limits in the first electrochemical cycle of $Li_{1.2}Ni_{0.13}Mn_{0.54}Co_{0.13}O_2$. *Nat. Commun.* **11**, 1252 (2020).

20 Eum, D. *et al.* Voltage decay and redox asymmetry mitigation by reversible cation migration in lithium-rich layered oxide electrodes. *Nat. Mater.* **19**, 419-427 (2020).

21 Ben Yahia, M., Vergnet, J., Saubanère, M. & Doublet, M.-L. Unified picture of anionic redox in Li/Na-ion batteries. *Nat. Mater.* **18**, 496-502 (2019).

22 Vergnet, J., Saubanère, M., Doublet, M.-L. & Tarascon, J.-M. The Structural Stability of P2-Layered Na-Based Electrodes during Anionic Redox. *Joule* **4**, 420-434 (2020).

23 Assat, G. *et al.* Fundamental interplay between anionic/cationic redox governing the kinetics and thermodynamics of lithium-rich cathodes. *Nat. Commun.* **8**, 2219 (2017).

24 Assat, G., Delacourt, C., Corte, D. A. D. & Tarascon, J.-M. Editors' Choice—Practical Assessment of Anionic Redox in Li-Rich Layered Oxide Cathodes: A Mixed Blessing for High Energy Li-Ion Batteries. *J. Electrochem. Soc.* **163**, A2965-A2976 (2016).

25 Assat, G., Iadecola, A., Delacourt, C., Dedryvère, R. & Tarascon, J.-M. Decoupling Cationic–Anionic Redox Processes in a Model Li-Rich Cathode via Operando X-ray Absorption Spectroscopy. *Chem. Mater.* **29**, 9714-9724 (2017).

26 McCalla, E. *et al.* Visualization of O-O peroxo-like dimers in high-capacity layered oxides for Li-ion batteries. *Science* **350**, 1516 (2015).

27 Chen, H. & Islam, M. S. Lithium Extraction Mechanism in Li-Rich Li_2MnO_3 Involving Oxygen Hole Formation and Dimerization. *Chem. Mater.* **28**, 6656-6663 (2016).

28 Chen, Z., Li, J. & Zeng, X. C. Unraveling Oxygen Evolution in Li-Rich Oxides: A Unified Modeling of the Intermediate Peroxo/Superoxo-like Dimers. *J. Am. Chem. Soc.* **141**, 10751-10759 (2019).

29 Rong, X. *et al.* Structure-Induced Reversible Anionic Redox Activity in Na Layered Oxide Cathode. *Joule* **2**, 125-140 (2018).

30 Mortemard de Boisse, B. *et al.* Highly Reversible Oxygen-Redox Chemistry at 4.1 V in $Na_{4/7-x}[\square_{1/7}Mn_{6/7}]O_2$ (□: Mn Vacancy). *Adv. Energy Mater.* **8**, 1800409 (2018).

31 Song, B. *et al.* Understanding the Low-Voltage Hysteresis of Anionic Redox in $Na_2Mn_3O_7$. *Chem. Mater.* **31**, 3756-3765 (2019).

32 Delmas, C., Fouassier, C. & Hagenmuller, P. Structural classification and properties of the layered oxides. *Physica B+C* **99**, 81-85 (1980).

33 Guo, S. *et al.* Understanding sodium-ion diffusion in layered P2 and P3 oxides via experiments and first-principles calculations: a bridge between crystal structure and electrochemical performance. *NPG Asia Mater.* **8**, e266-e266 (2016).

34 Du, K. *et al.* Exploring reversible oxidation of oxygen in a manganese oxide. *Energy Environ. Sci.* **9**, 2575-2577 (2016).

35 House, R. A. *et al.* Superstructure control of first-cycle voltage hysteresis in oxygen-redox cathodes. *Nature* **577**, 502-508 (2020).

36 Cao, X. *et al.* Restraining Oxygen Loss and Suppressing Structural Distortion in a Newly Ti-Substituted Layered Oxide P2-$Na_{0.66}Li_{0.22}Ti_{0.15}Mn_{0.63}O_2$. *ACS Energy Lett.* **4**, 2409-2417 (2019).

37 Yang, W. & Devereaux, T. P. Anionic and cationic redox and interfaces in batteries: Advances from soft X-ray absorption spectroscopy to resonant inelastic scattering. *J. Power Sources* **389**, 188-197 (2018).

38 Zhuo, Z. *et al.* Spectroscopic Signature of Oxidized Oxygen States in Peroxides. *J. Phys. Chem. Lett.* **9**, 6378-6384 (2018).

39 Somerville, J. W. *et al.* Nature of the “Z”-phase in layered Na-ion battery cathodes. *Energy Environ. Sci.* **12**, 2223-2232 (2019).

40 Yabuuchi, N. *et al.* New O2/P2-type Li-Excess Layered Manganese Oxides as Promising Multi-Functional Electrode Materials for Rechargeable Li/Na Batteries. *Adv. Energy Mater.* **4**, 1301453 (2014).

41 Singh, G., López del Amo, J. M., Galceran, M., Pérez-Villar, S. & Rojo, T. Structural evolution during sodium deintercalation/intercalation in $Na_{2/3}[Fe_{1/2}Mn_{1/2}]O_2$. *J. Mater. Chem. A* **3**, 6954-6961 (2015).

42 Hong, J. *et al.* Structural evolution of layered $Li_{1.2}Ni_{0.2}Mn_{0.6}O_2$ upon electrochemical cycling in a Li rechargeable battery. *J. Mater. Chem.* **20**, 10179-10186 (2010).

43 Myeong, S. *et al.* Understanding voltage decay in lithium-excess layered cathode materials through oxygen-centred structural arrangement. *Nat. Commun.* **9**, 3285 (2018).

44 Sathiya, M. *et al.* Origin of voltage decay in high-capacity layered oxide electrodes. *Nat. Mater.* **14**, 230-238 (2015).

45 Huang, Q. *et al.* Tailoring alternating heteroepitaxial nanostructures in Na-ion layered oxide cathodes via an in-situ composition modulation route. *Nano Energy* **44**, 336-344 (2018).

46 Yao, H.-R. *et al.* Designing Air-Stable O3-Type Cathode Materials by Combined Structure Modulation for Na-Ion Batteries. *J. Am. Chem. Soc.* **139**, 8440-8443 (2017).

47 Rong, X. *et al.* Anionic Redox Reaction-Induced High-Capacity and Low-Strain Cathode with Suppressed Phase Transition. *Joule* **3**, 503-517 (2019).

48 Sudayama, T. *et al.* Multiorbital Bond Formation for Stable Oxygen-Redox Reaction in Battery Electrodes. *Energy Environ. Sci.* **13**, 1492-1500 (2020).

49 Freire, M. *et al.* A new active Li–Mn–O compound for high energy density Li-ion batteries. *Nat. Mater.* **15**, 173-177 (2016).

50 Julien, C. M., Ait-Salah, A., Mauger, A. & Gendron, F. Magnetic properties of lithium intercalation compounds. *Ionics* **12**, 21-32 (2006).

51 Wu, J. *et al.* Dissociate lattice oxygen redox reactions from capacity and voltage drops of battery electrodes. *Sci. Adv.* **6**, eaaw3871 (2020).

52 Findlay, S. D. *et al.* Dynamics of annular bright field imaging in scanning transmission electron microscopy. *Ultramicroscopy* **110**, 903-923 (2010).

53 Wang, R. *et al.* Atomic Structure of Li_2MnO_3 after Partial Delithiation and Re-Lithiation. *Adv. Energy Mater.* **3**, 1358-1367 (2013).

54 Liberti, E. *et al.* Quantifying oxygen distortions in lithium-rich transition-metal-oxide cathodes using ABF STEM. *Ultramicroscopy* **210**, 112914 (2020).

55 Cramer, C. J., Tolman, W. B., Theopold, K. H. & Rheingold, A. L. Variable character of O—O and M—O bonding in side-on (η^2) 1:1 metal complexes of O_2. *Proc. Natl. Acad. Sci. U.S.A.* **100**, 3635 (2003).

56 Li, X. *et al.* Direct Visualization of the Reversible O^{2-}/O^{-} Redox Process in Li-Rich Cathode Materials. *Adv. Mater.* **30**, 1705197 (2018).

57 Wutthiprom, J., Phattharasupakun, N. & Sawangphruk, M. Turning Carbon Black to Hollow Carbon Nanospheres for Enhancing Charge Storage Capacities of $LiMn_2O_4$, $LiCoO_2$, $LiNiMnCoO_2$, and $LiFePO_4$ Lithium-Ion Batteries. *ACS Omega* **2**, 3730-3738 (2017).

58 Das, T. K., Couture, M., Ouellet, Y., Guertin, M. & Rousseau, D. L. Simultaneous observation of the O—O and Fe—O_2 stretching modes in oxyhemoglobins. *Proc. Natl. Acad. Sci. U.S.A.* **98**, 479 (2001).

59 Krebs, C., Edmondson, D. E. & Huynh, B. H. Demonstration of Peroxodiferric Intermediate in M-Ferritin Ferroxidase Reaction Using Rapid Freeze-Quench Mössbauer, Resonance Raman, and XAS Spectroscopies. *Methods Enzymol.* **354**, 436-454 (2002).

60 Malavasi, L., Galinetto, P., Mozzati, M. C., Azzoni, C. B. & Flor, G. Raman spectroscopy of AMn_2O_4 (A = Mn, Mg and Zn) spinels. *Phys. Chem. Chem. Phys.* **4**, 3876-3880 (2002).

61 Kresse, G. & Furthmüller, J. Efficiency of ab-initio total energy calculations for metals and semiconductors using a plane-wave basis set. *Comput. Mater. Sci.* **6**, 15-50 (1996).

62 Perdew, J. P., Burke, K. & Ernzerhof, M. Generalized Gradient Approximation Made Simple. *Phys. Rev. Lett.* **77**, 3865-3868 (1996).

63 Jain, A. *et al.* A high-throughput infrastructure for density functional theory calculations. *Comput. Mater. Sci.* **50**, 2295-2310 (2011).

Figures

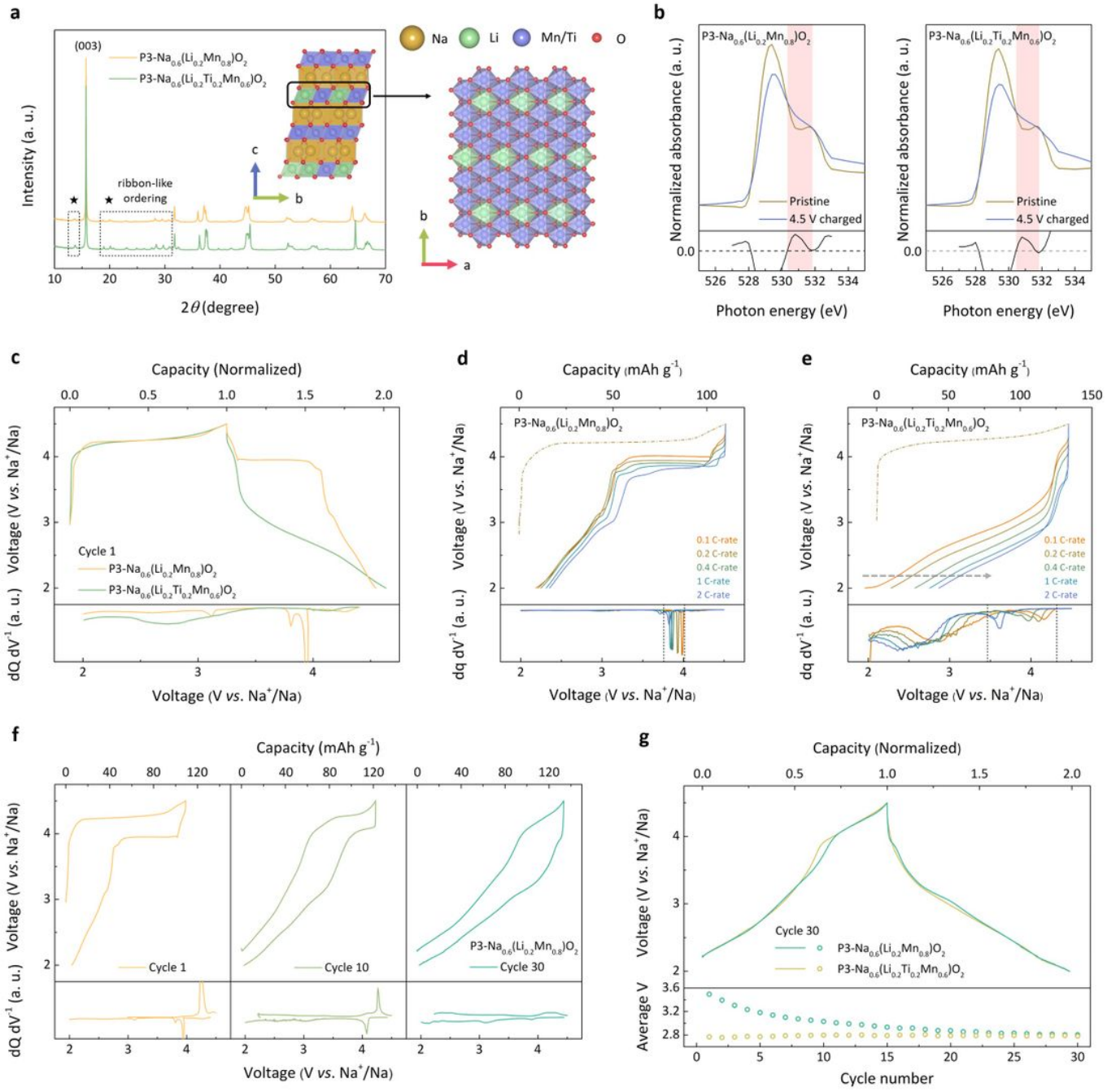

Figure 1

Structural and electrochemical properties of NLMO and NLTMO. a, HRPD patterns of NLMO and NLTMO with P3-type structure model. The superstructure peaks are located in the dotted regions in the diffraction patterns. Schematic illustrations of crystal structures of P3-type sodium layered oxides along the front and top views are shown together. b, STXM spectra of the O K-edge for the pristine and 4.5-V-charged NLMO (left) and NLTMO (right). The differential spectra between the pristine and 4.5-V-charged states are shown together. c, Normalized charge–discharge curves of NLMO and NLTMO cycled in the voltage range of 2.0–4.5 V. The bottom graph compares the dQ dV−1 curves during the initial discharge process. Electrochemical curves for d, NLMO and e, NLTMO for C-rates ranging from 0.1 to 2. In both graphs, the dotted charging curve corresponds to 0.2 C. The dQ dV−1 curves below more clearly illustrate the

contrasting behavior of the two materials. The dotted regions indicate the major change regions depending on the different rates. f, Charge-discharge profiles of NLMO for the 1st, 10th, and 30th cycles operated in the voltage window of 2.0–4.5 V. A comparison of the dQ dV−1 curves for the 1st, 10th, and 30th cycled NLMO is provided below the graph. g, Overlay of electrochemical curves for NLMO and NLTMO after 30 cycles. The average discharge voltage curves for 30 cycles are presented below.

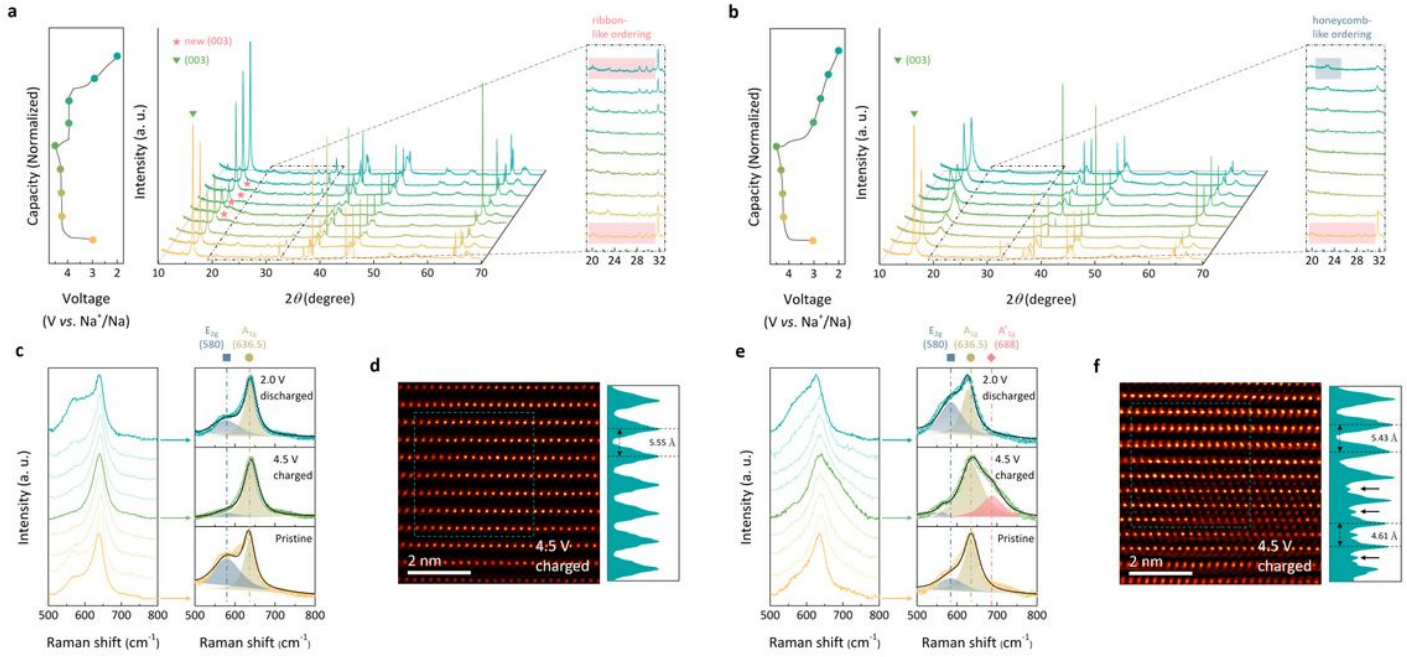

Figure 2

Comparison of out-of-plane cation disorder in NLMO and NLTMO. Ex-situ HRPD patterns of a, NLMO and b, NLTMO for each point in the electrochemical profiles. Magnified views of the patterns within the dotted regions are displayed on the right. The sharp peaks at 38, 44, and 64 correspond to those from Al foil. Ex-situ Raman spectra of c, NLMO and e, NLTMO for the same points as the HRPD measurements. The peak at 636.5 cm−1 (circle) is a signature of symmetric stretching (A1g) of the TM–O bond in layered structures, whereas the peak at 580 cm−1 (square) arises from asymmetric stretching (E2g) of the Na–O bond.41 Detailed deconvolution results of Raman spectra for the pristine, 4.5-V-charged, and 2.0-V-discharged states of NLMO and NLTMO are presented on the right, respectively. The yellow (circle), blue (square), and red shaded peaks (rhombus) are associated with the original TM–O (A1g), Na–O (E2g), and defective TM–O vibrations (A’1g), respectively. HAADF-STEM images along the [010] zone axis for the 4.5-V-charged d, NLMO and f, NLTMO. The graphs on the right are the HAADF signal profiles of the regions enclosed by the dotted lines in the STEM images.

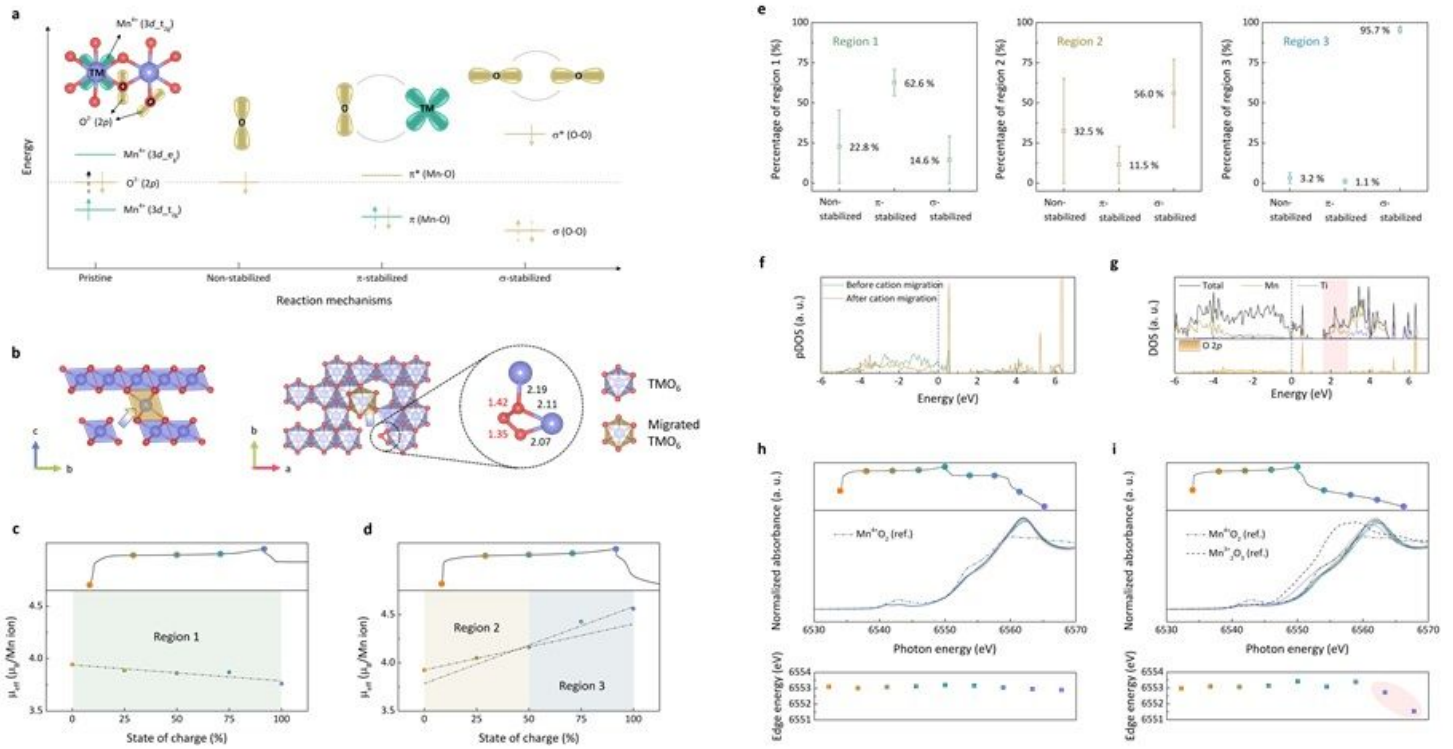

Figure 3

Redox stabilization mechanisms of oxidized lattice oxygen. a, Schematic illustration of molecular orbital diagram for the pristine state and three different charged cases. In the pristine state, the dotted black arrow of O2– (2p) corresponds to the electron to be extracted upon charging. The yellow line and arrow are associated with O ions, whereas the green ones are attributed to Mn ions. The green and yellow dotted arrows indicate electrons of coordinated Mn and O ions, respectively. In the case of the non-stabilized oxygen, the total magnetization should simply increase with the oxygen oxidation due to the creation of this localized hole. On the other hand, when the oxygen has the appreciable interaction with a neighboring Mn, the holes in the oxygen 2p state can be delocalized through the formation of a new π state, where the unpaired electrons in the Mn t2g states is also shared. In this case, the total magnetization would decrease whenever oxygen holes are generated. Alternatively, the holes of oxidized oxygen can be delocalized through the dimerization with a nearby lattice oxygen, which is known to be preceded by a metal–oxygen decoordination process.17 The oxygen dimerization creates the σ states, and the unpaired electron would occupy the anti-bonding σ* state, increasing the magnetic moments of the system.15,28 b, Computational prediction of O–O dimerization stabilized by out-of-plane cation disorder. The schemes show the out-of-plane structural disordering along the front and top views, and the arrow in the schemes indicates the cation-migration pathway. The yellow TMO6 octahedra represents the out-of-plane migrated TM. The bond lengths of O–O and adjacent TM–O are specified in the magnified view. Effective magnetic moments of c, NLMO and d, NLTMO for SOC ranging from 0% to 100% during the initial charge process. e, Quantitative deconvolution results of the slopes for the three regions; Region 1, Region 2, and Region 3 in c and d. The values in the figures represent the percentages of each of the respective mechanisms (Average values). f, pDOS of individual oxygen atoms involved in O–O

dimerization before and after cation-migration process in the fully charged NLTMO structure. g, DOS of total, Mn, and Ti atoms in the same model structure with cation migration. pDOS of O2p states is concomitantly plotted below for comparison. The dotted lines in the graphs indicate the Fermi level. Mn K-edge XANES spectra for h, NLMO and i, NLTMO for nine points in the electrochemical curve. The additional spectra in the graphs are reference spectra for the oxidation states of 3+ and 4+ with Mn2O3 and MnO2 materials, respectively. Half-edge energy positions of NLMO and NLTMO during the successive charge and discharge process are presented below, respectively.

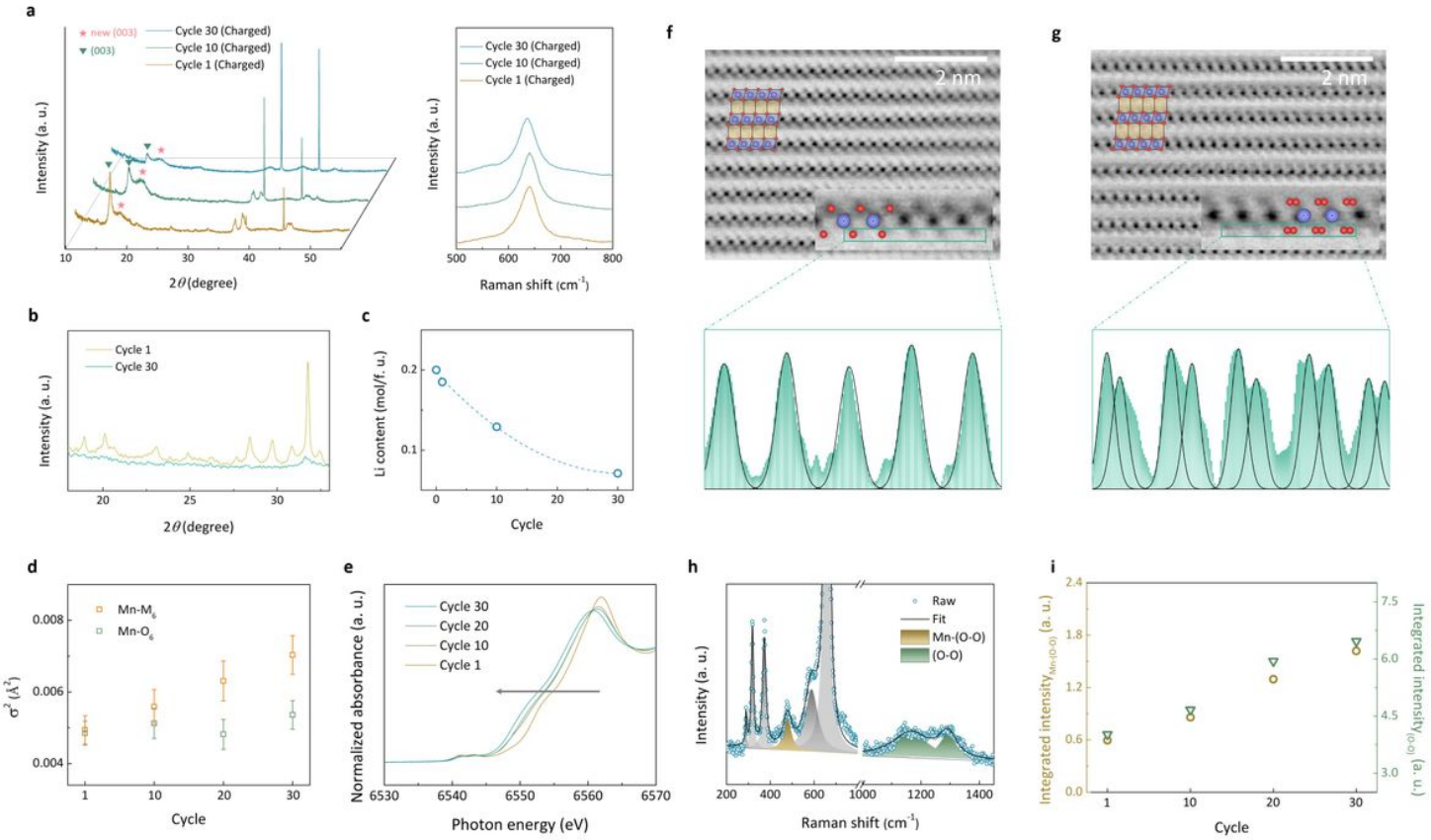

Figure 4

Oxygen dimerization generated by in-plane cation disorder in NLMO. a, Ex-situ HRPD patterns and Raman spectra of the 1st charged, 10th charged, and 30th charged NLMO. The sharp peaks at 38 and 44 correspond to those from Al foil. b, Comparison of the pristine and 1- and 30-cycled NLMO for the superstructure peaks. c, Remaining Li content in the charged NLMO electrode over the extended cycles d, Fitting results of Debye–Waller factor for the first and second shells of the Mn ions. The data were collected every 10 cycles. e, Mn K-edge XANES spectra of the 1-, 10-, 20-, and 30-cycled NLMO. The arrow in the graph highlights the drastic shift toward low energy with cycling. ABF-STEM images along the [010] zone axis for the 4.5-V-charged NLMO in f, cycle 1 and g, cycle 30. The blue and red spheres represent Mn and O features, respectively. The blue and yellow polyhedra represent Mn octahedral sites and vacant Na prismatic sites, respectively, in the P3-type stackings. The graphs below show the ABF signal profiles of the regions enclosed by the dotted squares in the STEM images. h, Raman spectrum of the 30th charged NLMO and fitting results with several individual peaks. The newly emerged yellow and green peaks after

cycling correspond to the Mn–(O–O) and (O–O) vibrations, respectively. The grey peaks arise from the well-known 3F2g, E2g, and A1g vibration modes, respectively.41,60 i, Variation of the integrated intensity for the Mn–(O–O) and (O–O) vibrations upon cycling of the NLMO electrode.

Supplementary Files

This is a list of supplementary files associated with this preprint. Click to download.

- SupplementaryInformation.docx